Preprint:
Castellanos-Reyes, José Ángel, Zeiger, Paul, Bergman, Anders et al. (4 more authors) (2023) Unveiling the impact of temperature on magnon diffuse scattering detection in scanning transmission electron microscopy. [Preprint]

arXiv:2302.11462v1 [cond-mat.mtrl-sci] 22 Feb 2023

Unveiling the impact of temperature on magnon diffuse scattering detection in scanning transmission electron microscopy

José Ángel Castellanos-Reyes,[1,*] Paul Zeiger,[1] Anders Bergman,[1] Demie Kepaptsoglou,[2,3] Quentin M. Ramasse,[2,4,5] Juan Carlos Idrobo,[6] and Ján Rusz[1,†]

[1] *Department of Physics and Astronomy, Uppsala University, Box 516, 75120 Uppsala, Sweden*
[2] *SuperSTEM Laboratory, SciTech Daresbury Campus, Daresbury WA4 4AD, United Kingdom*
[3] *Department of Physics, University of York, York YO10 5DD, United Kingdom*
[4] *School of Chemical and Process Engineering, University of Leeds, Leeds LS2 9JT, United Kingdom*
[5] *School of Physics and Astronomy, University of Leeds, Leeds LS2 9JT, United Kingdom*
[6] *Materials Science and Engineering Department, University of Washington, Seattle, Washington 98195, USA*

(Dated: February 23, 2023)

Magnon diffuse scattering (MDS) signals could, in principle, be studied with high spatial resolution in scanning transmission electron microscopy (STEM), thanks to recent technological progress in electron energy loss spectroscopy. However, detecting MDS signals in STEM is technically challenging due to their overlap with the much stronger thermal diffuse scattering (TDS) signals. In bcc Fe at 300 K, MDS signals greater than or comparable to TDS signals occur under the central Bragg disk, well into a currently inaccesible energy-loss region. Therefore, to successfully detect MDS in STEM, it is necessary to identify conditions in which TDS and MDS signals can be distinguished from one another in regions outside the central Bragg disk. Temperature may be a key factor due to the distinct thermal signatures of magnon and phonon signals. In this work, we present a study on the effects of temperature on MDS and TDS in bcc Fe—considering a detector outside the central Bragg disk—using the frozen phonon and frozen magnon multislice methods. Our study reveals that neglecting the effects of atomic vibrations causes the MDS signal to grow approximately linearly up to the Curie temperature of Fe, after which it exhibits less variation. The MDS signal displays an alternating behavior due to dynamical diffraction, instead of increasing monotonically as a function of thickness. The inclusion of the Debye-Waller factor (DWF) causes the linear growth of the MDS signal to change to an oscillatory behavior that exhibits a predominant peak for each thickness, which increases and shifts to higher temperatures as the thickness increases. In contrast, the TDS signal grows more linearly than the MDS signal (with DWF) but still exhibits appreciable dynamical diffraction effects. An analysis of the signal-to-noise ratio (SNR) shows that the MDS signal can be a statistically significant contribution to the total scattering intensity under realistic measurement conditions and reasonable acquisition times. For example, our study found that an SNR of 3 can be achieved with a beam current of 1 nA in less than 30 minutes for a bcc Fe sample with a thickness of 16.072 nm at a temperature of 500 K.

I. INTRODUCTION

Scanning transmission electron microscopy (STEM) is a powerful and versatile technique to study and characterize micro- and nanostructures [1]. Recent progress in STEM monochromators and spectrometers has made it possible to perform electron energy loss spectroscopy (EELS) with sub-10 meV energy resolution at nanometric and atomic spatial resolutions [2–5]. This has opened the possibility for high-spatial-resolution STEM-EELS studies of elementary excitations in the zero-to-few-hundreds meV range, such as molecular vibrations, infrared plasmons, and phonons [6]. It has been pointed out that high spatial resolution STEM-EELS could, in principle, be performed also for magnons [7–9], since their excitation energies lie in the same range [10].

Magnons are quanta of collective spin excitations (quantized spin waves), pictured semiclassically as waves of precessing magnetic dipole moments [10]. These quasiparticles lie at the core of the current understanding of the ordered magnetism of solids [11, 12]. Therefore, studying magnons at high spatial resolution in STEM would be relevant not only for magnetic solid-state technologies (such as spintronics, spin caloritronics [13, 14], and magnonics [15]) but also for the foundations of solid-state magnetism.

Detecting magnon signals in STEM is technically challenging, since they are typically orders of magnitude less intense than the so-called thermal diffuse scattering (TDS) signals [7, 9]—produced by the inelastic scattering of the electron probe due to lattice vibrations (i.e., phonons). For example, in Ref. [7] it was reported that the simulated TDS signal for bcc Fe at 300 K is four orders of magnitude greater than the corresponding magnon diffuse scattering (MDS) signal. Moreover, the simulations of Ref. [9] for the same system showed that MDS signals greater than or comparable to TDS signals are found only for scattering angles smaller than 0.5 mrad, under the central Bragg disk. This region corresponds—through the dispersion relation—to

* angel.castellanos.research@gmail.com
† jan.rusz@physics.uu.se

magnons with energies below 10 meV [10], practically on the current energy resolution limit of monochromated EELS [2–5].

Hence, to achieve MDS detection in STEM at high-spatial resolution, it is necessary to find conditions in which MDS and TDS signals can be told apart. In particular, as has been argued in Ref. [7], temperature could play a decisive role for this purpose.

In this Article, we investigate the behavior of MDS at different temperatures and explore the possibility of temperature-aided detection of MDS in STEM. Employing the prototypical bcc Fe as the magnetic system and the methodology developed in Ref. [7], we investigate the temperature dependence of simulated MDS signals. From the studied cases, we establish optimal combinations of temperature and sample thickness having the highest MDS signals. In particular, we focus on signals surrounding the central Bragg disk to explore and address the challenge reported in Ref. [9]. Finally, we compare our results with TDS simulations and discuss the feasibility of MDS detection in STEM.

II. METHODS

To simulate the inelastic electron-probe scattering on a specimen at a certain temperature in STEM, it is necessary to have a model for the specimen at the considered temperature and to implement a method for electron-beam propagation through it. In this work, the inelastic signals—TDS and MDS—of ferromagnetic bcc Fe are obtained following the methodology of Ref. [7]. Explicitly, the TDS signals are calculated via the frozen phonon multislice (FPMS) method [16] and the MDS signals via the analogous frozen magnon multislice (FMMS) method, originally introduced in Ref. [7]. These methods are named “frozen” because each electron from the STEM probe travels with a relativistic speed, interacting with the specimen in a time on the order of tens of attoseconds, at which the motion of atoms and their magnetic moments looks practically “frozen.”

To simulate the electron-beam propagation through the specimen in FPMS, the conventional multislice method [17] is employed. In FMMS, to account for the effects of spins and magnetism, the Pauli multislice method [18, 19] is utilized. We employed an in-house developed software for both multislice methods.

For TDS calculations at a given temperature, the magnetic moments of Fe atoms are completely ignored, and the dynamics of the Fe atomic vibrations (phonons) are obtained through molecular dynamics (MD) simulations. Meanwhile, for the MDS calculations, atomistic spin dynamics (ASD) [10] simulations are employed to obtain the dynamics of the magnons—i.e. the evolution of the precessing magnetic moments of Fe atoms (of imposed constant magnitude)—assuming that the atomic positions are kept fixed. ASD simulations accurately model the dynamics of thermally excited magnetic moments configurations in a manner analogous to how MD does for atomic vibrations.

In FPMS, the TDS signal is obtained by sampling over the possible atomic displacements configurations [16, 20]. Analogously, the MDS signal in FMMS is computed by sampling over the magnetic moments configurations [7]. In both FPMS and FMMS, the inelastic signal at the diffraction plane, for a given temperature, is calculated as the difference between the so-called *incoherent* and *coherent* intensities [7, 21, 22]. On the one hand, the incoherent intensity—corresponding to the total scattered signal $I_{\rm tot}$ in the diffraction plane—is the average, over all samples, of the exit wavefunctions' intensities (squared amplitudes). On the other hand, the coherent intensity is the squared amplitude of the averaged exit wavefunctions, and it corresponds to the purely elastic scattering signal $I_{\rm ela}$ in the diffraction plane. Therefore, the inelastic signal $I_{\rm ine}(T)$ at temperature T is given by

$$I_{\rm ine}(T) = I_{\rm tot}(T) - I_{\rm ela}(T), \tag{1}$$

where “ine” stands for MDS in the case of FMMS, and TDS in the case of FPMS.

We have chosen ferromagnetic bcc Fe as our model system because it is a prototypical magnetic material for which magnons have been detected using electron beams [23]. Moreover, the methodology discussed above has already been tested in Ref. [7] for bcc Fe.

For the calculations, we have employed supercells $\mathcal{S}_t$ consisting of $20 \times 20 \times (14t)$ repetitions of the bcc Fe unit cell (in x, y, and z directions, respectively; see Fig. 1), with $t \in \{1, 2, 3, 4, 5\}$ to account for five different thicknesses, of dimensions $5.74 \times 5.74 \times (4.018t)$ nm^3, containing $11200t$ atoms. Periodic boundary conditions were considered in x, y, and z directions.

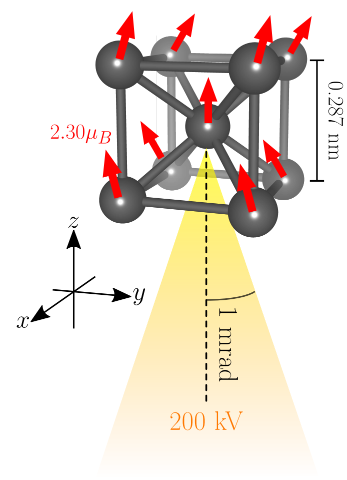

FIG. 1. Scheme of the system under consideration. A 200 kV aberration-free STEM electron probe, propagating in z direction with 1 mrad convergence semiangle, illuminates a unit cell of bcc Fe at a certain temperature, with lattice parameter 0.287 nm and 2.30 μ_B atomic magnetic moment (μ_B is the Bohr magneton).

To implement FMMS, we generated a representative sampling of the magnetic moments configurations from ASD simulations using the `UppASD` code [10, 24]. We considered the Heisenberg Hamiltonian with exchange interactions and magnetic moments computed ab initio with the scalar-relativistic `SPRKKR` code [25]. The magnitude of Fe magnetic moments was 2.30 μ_B (where μ_B is the Bohr magneton). To account for the effect of the microscope's objective lens, we have included a 1 T external static magnetic field oriented along the positive z direction. A sample of 101 configurations per temperature—from 0 K to 1700 K—was obtained by taking a *snapshot* (i.e., a static configuration), every 10 fs, out of an ASD simulation with a 0.1 fs time step. To minimize the correlation between different snapshots, we set a large Gilbert damping parameter $\alpha = 0.5$ in the simulations. Then, for each snapshot, we performed a Pauli multislice simulation. Finally, the MDS signal at a given temperature was obtained using the coherent and incoherent averages (over all the snapshots) as in Eq. (1). A discussion about the level of convergence of our calculations in terms of the accuracy of the computed averages is presented in Appendix A.

Analogously, we performed FPMS simulations using snapshots sampled from trajectories of constant temperature MD simulations ("NVT ensemble") in the `LAMMPS` software [26, 27][28]. The size of the supercell was set in the same way as in the `UppASD` calculations described above. The simulations were run using a Nosé-Hoover thermostat, which maintained the specified temperature with a temperature damping parameter $T_{\text{damp}} = 100$ fs. In order to account for thermal expansion, the average lattice parameter in the NVT ensemble simulations was determined from constant temperature and constant pressure MD simulations ("NPT ensemble") for each temperature. The time step of the MD simulation was set to 1 fs and the interatomic forces between Fe atoms were described by a so-called *embedded-atom method* (EAM) potential [29]. Similar to the case of the FMMS simulations, we sample 101 configurations per temperature from the MD trajectories in the NVT ensemble by taking a snapshot of the *atomic positions* every 1000 fs after an initial thermal equilibration time of 10000 fs.

In the conventional and Pauli multislice simulations, following the discussion of Ref. [7] regarding the resolution of inelastic signals in the diffraction plane, we have employed a 200 kV aberration-free electron probe focused on the entrance surface of the supercell, with a 1 mrad convergence semiangle, propagating in z direction (see Fig. 1). For the supercell $\mathcal{S}_t$, the multislice calculations were performed on a regular grid $\mathcal{G}_t$ consisting of $1000 \times 1000 \times (420t)$ points in x, y, and z directions, spanning the entire supercell.

The magnetic field $\mathbf{B}(\mathbf{r})$ and vector potential $\mathbf{A}(\mathbf{r})$ produced by Fe magnetic moments on a given snapshot (used for multislice simulations) were calculated using the parametrization by Lyon and Rusz [30], which has been successfully benchmarked against density functional theory calculations of bcc Fe.

For the electrostatic potential $V(\mathbf{r})$ of Fe atoms, we employed the parametrization by Peng et al. [31]. Additionally, we implemented the Debye-Waller factor (DWF) [11] into $V(\mathbf{r})$ to account for the attenuation of elastic signals due to thermal motions in FMMS simulations [32]. The mean-squared displacements (MSD) used for the implementation of the DWF were computed from a running average of the MSD, computed at every time step in the aforementioned MD simulations in the NVT ensemble, and are presented in Table I in Appendix B.

In all cases, $V(\mathbf{r})$, $\mathbf{B}(\mathbf{r})$, and $\mathbf{A}(\mathbf{r})$ were computed in the gridpoints of $\mathcal{G}_t$ surrounding each Fe atom up to a specified cutoff distance r_{cut}, above of which all are set to zero. The specific value of r_{cut} used in each case was chosen as a compromise between numerical accuracy and computational resources demand, see Appendix C.

III. EFFECTS OF THE TEMPERATURE ON MDS AND FEASIBILITY OF TEMPERATURE-AIDED DETECTION

The aim of this work is to investigate the behavior of MDS at different temperatures, particularly, to explore the possibility of temperature-aided MDS detection in STEM. Therefore, we start our study in Subsection III A presenting the general features of the resulting electron-probe diffraction patterns. At this first stage, we select a STEM detector that collects relevant MDS signals surrounding the central Bragg disk and study these signals as a function of temperature in the following.

In Subsection III B we study the MDS while completely ignoring the effects of atomic vibrations. Therein, we present the results of the MDS as a function of temperature for all the specimen thicknesses considered.

One of the effects of atomic vibrations is the attenuation of elastic signals as the scattering angle and/or the temperature increase [11]. This effect can be introduced in static-lattice calculations by implementing the Debye-Waller factor (DWF). Hence, to continue our investigations, in Subsection III C we study how the DWF changes the MDS signal as a function of temperature, in the first approximation to the effects caused by atomic vibrations.

To complement, in Subsection III D we show simulations of the TDS signal (ignoring completely the magnetic moments of Fe) and contrast it with the MDS signal. Finally, in Subsection III E we discuss the implications of our findings for the successful detection of MDS in STEM.

All the intensities presented in the figures of this work are divided by the total intensity of the incident electron beam integrated over the whole diffraction plane, I_0, to show dimensionless results. Moreover, when plotted in regions of the diffraction plane, as a function of the scattering angle, they actually correspond to intensities integrated over pixels. This is the case for Figs. 2, 4, 7, and 8. The size of a pixel in our calculations (that can be computed from the parameters described in Section II) is 0.19 mrad^2.

A. MDS diffraction patterns and selection of an annular dark-field detector

We simulated MDS signals for different temperatures and thicknesses fixing the atomic positions, both when including and ignoring the DWF. The relevant features of all the resulting diffraction patterns can be appreciated in Fig. 2, showing results for bcc Fe of 20.09 nm thickness at 1700 K, including the DWF.

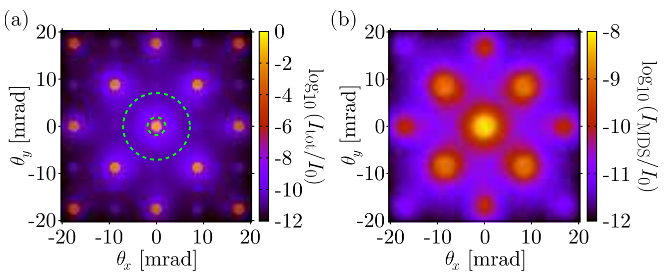

FIG. 2. Diffraction patterns calculated for bcc Fe of 20.09 nm thickness at 1700 K, including the Debye-Waller factor (DWF). (a) Total signal $\log_{10}(I_{\rm tot}/I_0)$ [I_0 denotes the total intensity of the incident electron beam integrated over the whole diffraction plane] and annular dark-field detector (ADF; shown in green dashed lines). (b) Magnon diffuse scattering (MDS) signal $\log_{10}(I_{\rm MDS}/I_0)$.

The general behavior of the total signal is illustrated in Fig. 2(a), showing $\log_{10}(I_{\rm tot}/I_0)$. The total signal consists of Bragg disks, alternating on high and low (forbidden reflections) intensities, with low-intensity lobes surrounding the high-intensity Bragg disks.

The MDS signal, $\log_{10}(I_{\rm MDS}/I_0)$, computed from Eq. (1), is shown in Fig. 2(b). In particular, it can be appreciated that the MDS signal is concentrated around the high-intensity Bragg disks, vanishing away from the center of the diffraction plane. We employed $r_{\rm cut} = 1$ nm in Fig. 2 for a better resolution of the MDS near the Bragg disks (see Appendix C). In particular, the highest MDS signal is located within the central Bragg disk, in agreement with Ref. [9]. Therefore, for experimental detection, it is relevant to analyze the MDS signal at small scattering angles surrounding the central Bragg spot.

Thus, to study the effects of temperature, we considered an annular dark-field (ADF) detector [17] of inner collection semiangle 2 mrad and outer collection semiangle 7 mrad [illustrated by the green dashed lines in Fig. 2(a)]—to avoid all Bragg disks, including the forbidden reflections. Hence, this detector collects only the MDS signal. In particular, as discussed in Appendix C, the calculations in this ADF detector are already converged at $r_{\rm cut} = 0.4$ nm—having MDS signals two orders of magnitude greater than the error coming from the averaging process (see Appendix A). Therefore, in the following, we study the effects of temperature on the signals collected by the aforementioned ADF detector using $r_{\rm cut} = 0.4$ nm.

B. MDS neglecting the effect of the atomic vibrations

In the top panel of Fig. 3, we show the simulated MDS signals as a function of temperature for the five different thicknesses considered in this work (in all cases, the continuous lines joining the computed values are only a guide to the eye). Specifically, we present $I_{\rm MDS}/I_0$ collected by the selected ADF detector up to 1700 K (the melting temperature of our system is around 1800 K). It can be appreciated in this panel that, for all thicknesses, the MDS signal grows approximately linearly up to ≈ 1100 K, corresponding to the Curie temperature ($T_{\rm C}$) of our samples. Above $T_{\rm C}$, the linear increment stops, giving place to a less-varying behavior. These features are consistent with the semiclassical picture of the interaction, in which the MDS signal would increase with the randomness in the orientation of the magnetic moments (this randomness reaches its maximum for $T \geq T_{\rm C}$).

It could be expected that the MDS signal increases with the thickness. However, in the top panel of Fig. 3, the signal corresponding to the thickness 8.036 nm is greater than the one of 12.054 nm. Also, the results of 16.072 nm are greater than those of 20.090 nm. This alternating behavior is due to dynamical diffraction (multiple scattering) [1]. In particular, increasing the thickness of the specimen for the electron beam propagation can lead to constructive and destructive interference conditions for the coherent intensity that are not present at the lowest thickness.

C. Effects of the Debye-Waller factor on MDS

The effects of including the DWF in MDS calculations can be appreciated in the bottom panel of Fig. 3, showing the signals collected by the chosen ADF detector in this case (in the same format as in the top panel of the same figure).

For the thinnest specimen considered (4.018 nm), the ADF-collected signal in the bottom panel of Fig. 3 again grows linearly up to $T_{\rm C}$, saturating at a slightly higher value than in the top panel. However, the higher sample thicknesses display a qualitatively different temperature dependence, in which the saturation and linearity disappear. In the specimens with thicknesses 8.036 nm, 12.054 nm, and 16.072 nm, the ADF-collected signal displays an oscillatory behavior, presenting a dominant peak for each thickness. This peak increases and shifts to higher temperatures as the thickness increases. Meanwhile, in the thickest specimen (20.090 nm), apart from these features, there is an additional smaller oscillation

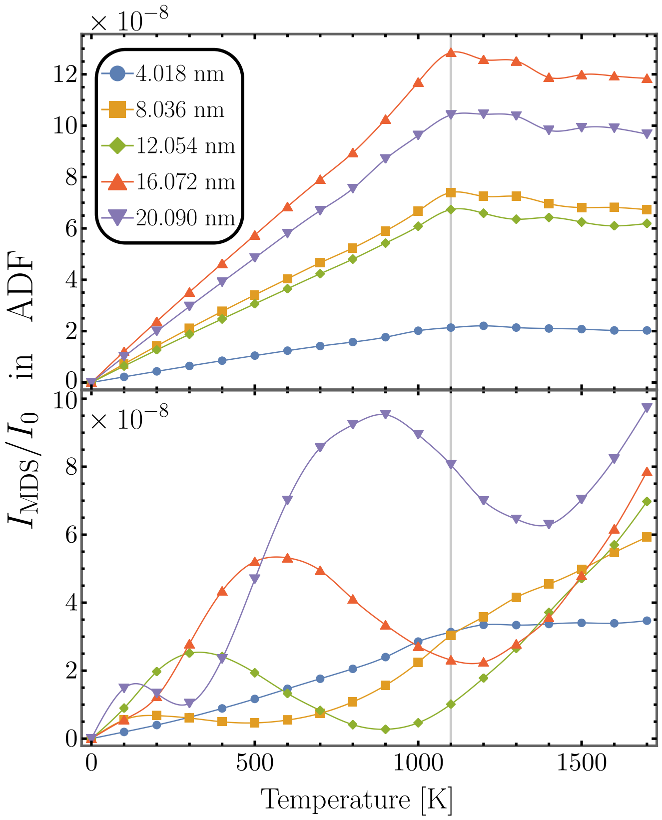

FIG. 3. MDS signals collected by the selected ADF detector for bcc Fe of different thicknesses (indicated in the legend of the top panel) as a function of temperature. The top panel shows I_{MDS}/I_0 neglecting the effect of the atomic vibrations, while the bottom panel includes the effects of the DWF. The gray vertical line indicates the Curie temperature of the samples. Solid lines joining the computed values are only a guide to the eye.

at low temperatures. Notably, the highest signal is obtained at the highest temperature, 1700 K, in all the studied cases.

The changes between the behavior of the MDS signals in the top and bottom panels of Fig. 3 come from the fact that the DWF varies with temperature—see Appendix B. An effect of the DWF is to reduce the probability that the electron probe scatters to higher angles. This reduction becomes stronger as the temperature increases [11]. Therefore, the DWF will modify the interference effects that produced the alternating (thickness) behavior in the case of the top panel of Fig. 3, where there was no DWF. In general, the dynamical diffraction [1], which affects the thickness dependence of the electron scattering signals, will be modified by the DWF. Hence, it is the temperature dependence of dynamical diffraction induced by the DWF that is responsible for the behavior of MDS in the bottom panel of Fig. 3.

D. Comparison between MDS and TDS

In Ref. [7] it was reported that the TDS signal was typically at least four orders of magnitude greater than the corresponding TDS signal at 300 K. We have found that this is also the case at the different temperatures and thicknesses considered in this work. This is illustrated in Fig. 4 showing vertical profiles of the TDS and MDS (including the DWF) signals through the center of the diffraction plane (i.e., as a function of the scattering angle θ_y, with $\theta_x = 0$).

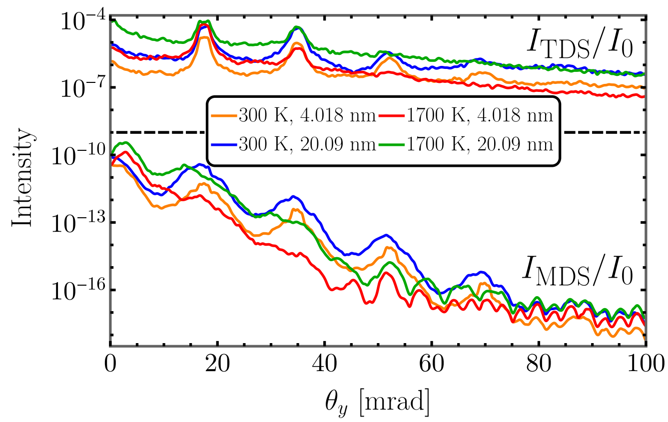

FIG. 4. I_{MDS}/I_0 (including the DWF) and I_{TDS}/I_0 as a function of the scattering angle θ_y, with $\theta_x = 0$, for bcc Fe—at 300 K and thickness 4.018 nm (orange curves), at 300 K and thickness 20.09 nm (blue curves), at 1700 K and thickness 4.018 nm (red curves), and at 1700 K and thickness 20.09 nm (green curves). In all cases, $r_{\text{cut}} = 0.4$ nm has been used. The TDS signals, always greater than the corresponding MDS signals, are located in the upper portion of the plot (above the horizontal black dashed line), while the MDS ones are in the lower portion.

Specifically, in Fig. 4 we show I_{TDS}/I_0 and I_{MDS}/I_0 for the thickest (blue and green curves) and the thinnest (orange and red curves) bcc Fe samples at 300 K (in orange and blue curves) and 1700 K (in red and green curves). In all cases, $r_{\text{cut}} = 0.4$ nm has been used. We have employed the same colors for the corresponding MDS and TDS signals, since they are well separated (we have included a horizontal black dashed line dividing them). In particular, it can be appreciated that the difference between the TDS and MDS signals becomes even larger at higher scattering angles. Therefore, the region of interest for MDS detection—now in the presence of the TDS signal—is again that of small scattering angles. This, together with avoiding the Bragg disks, supports the choice of the same ADF detector used for the MDS studies in the previous subsections.

In the top panel of Fig. 5, we present the signal I_{TDS}/I_0 collected by the ADF detector, as a function of temperature, for the different sample thicknesses, in the same format as in Fig. 3. It can be observed that the TDS signal is about five orders of magnitude greater than the corresponding MDS signal (see Fig. 3). In contrast to the MDS case, the TDS curves grow more linearly with the temperature, but dynamical diffraction effects can also be appreciated. In particular, for the thickness 20.090 nm, a weak oscillatory component in the temperature dependence of I_{TDS} can be appreciated.

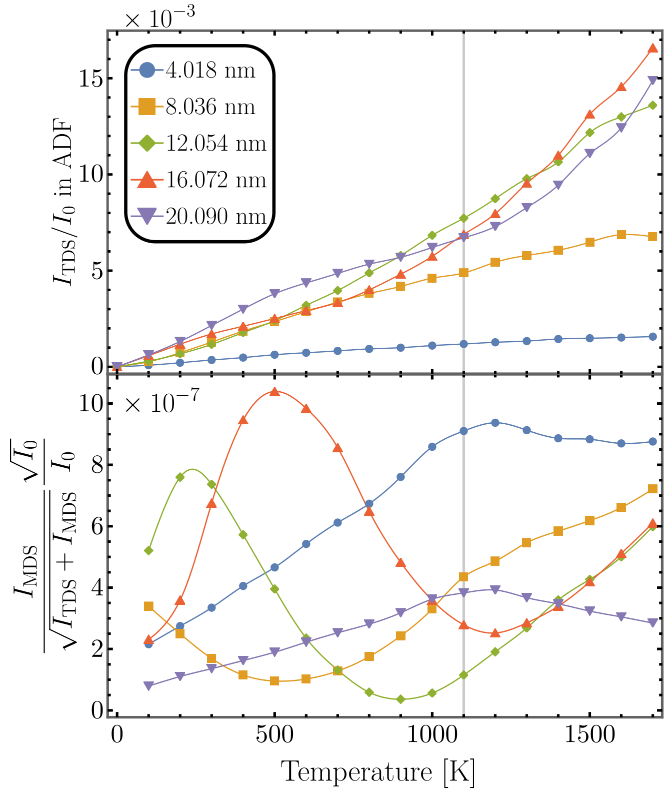

FIG. 5. Top panel: I_{TDS}/I_0 collected by the ADF detector as a function of temperature in the same format as Fig. 3. Bottom panel: signal-to-noise ratio (SNR) evaluated for a dose of one electron. Line colors follow the legend of the top panel.

To determine the optimal combination of temperature and sample thickness for MDS detection, it is relevant to consider the signal-to-noise ratio (SNR) in the ADF detector, which is given in this case by

$$\mathrm{SNR} = \left(\frac{I_{\mathrm{MDS}}}{\sqrt{I_{\mathrm{TDS}} + I_{\mathrm{MDS}}}} \frac{\sqrt{I_0}}{I_0} \right) \sqrt{\frac{i_b t_a}{e}}, \qquad (2)$$

where i_b is the STEM-electron-beam current, t_a is the acquisition time, e is the elementary electric charge, and the inelastic intensities are those collected by the detector.

In the bottom panel of Fig. 5 we show the SNR evaluated for an electron dose of one electron [i.e., for $i_b t_a/e = 1$ in Eq. (2)] for all the temperatures and sample thicknesses considered. It can be observed that the optimal detection setup corresponds to a sample of 16.072 nm thickness at 500 K. This is a consequence of the contrasting behavior of the MDS and TDS signals for the 16.072 nm specimen around 500 K, which can be appreciated in the top panel of Fig. 5 and the bottom panel of Fig. 3. While the MDS has a peak at 500 K, with a distinctive concave behavior, the TDS presents a slightly convex behavior in the same region. Could this change be detected and resolved in current STEM machines? A positive answer would imply a method for temperature-aided detection of MDS in STEM.

A typical criterion for successful detection conditions in STEM is to have at least SNR = 3 [33], while in general signal processing SNR = 5 criterion is used [34]. Therefore, using Eq. (2) for the sample of 16.072 nm thickness at 500 K, we present in Fig. 6 log-log plots of i_b as a function of t_a giving SNR = 3 and SNR = 5.

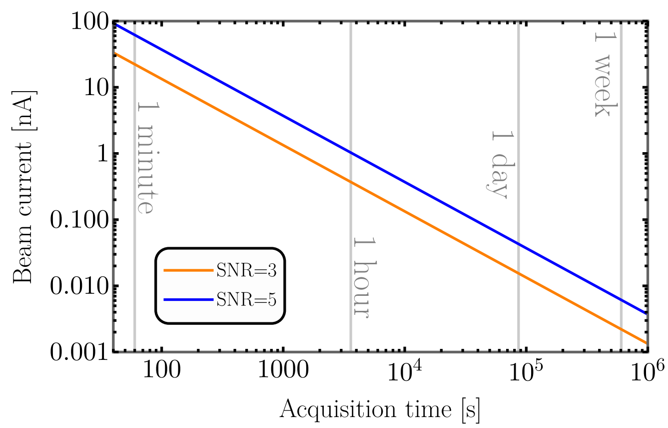

FIG. 6. Log-log plots of the electron beam current i_b as a function of the acquisition time t_a—computed from Eq. (2)—producing signal-to-noise ratios (SNR) of 3 and 5, for bcc Fe of 16.072 nm thickness at 500 K.

It is worth mentioning that existing STEM machines vary from some of which have low i_b, on the order of pA, to others capable of routinely working well above 1 nA [35–37]. Therefore, it can be appreciated in Fig. 6 that our calculations predict large yet reasonable acquisition times for realistic conditions (below one hour for beam currents over 1 nA). For example, it is predicted that a SNR = 3 could be obtained in less than 30 min. using a 1 nA electron probe. Also, it is worth noticing that for tens of pA, the acquisition times are less than one day.

E. Discussion

We have shown that, in our simulations, there are optimal detection conditions at which I_{MDS} can be statistically significant at reasonable acquisition times. Therefore, there might exist experimental configurations allowing for temperature-aided detection of MDS in STEM.

However, we have not put forward an explicit method to separate the two contributions, I_{TDS} and I_{MDS}. A possible starting point in this endeavor could rely on the difference in the concavity of the signals at the optimal conditions, pointed out in the previous subsection. In particular, it could be useful to fit with Gaussian functions the experimental ADF-collected signals at different temperatures to detect the I_{MDS} peaks. Also, given the oscillatory behavior of I_{TDS} and I_{MDS}, having different periodicity, it might be relevant to track such periods in the Fourier transforms of the measured temperature dependences. Moreover, rotating the samples' magnetization could be attempted, since it may influence I_{MDS}, leaving I_{TDS} unaltered.

Nevertheless, independently of any specific detection strategy, we consider that the main finding of our work is that, under realistic measurement conditions, the I_{MDS} signal can become a statistically significant contribution to the total scattering intensity within a suitably chosen detector.

To further bridge the gap toward successful MDS detection in STEM, it would be valuable to perform energy-resolved STEM studies. For that matter, a theoretical methodology allowing for MDS simulations with energy resolution would be of utmost relevance. Nevertheless, the findings reported in this work could likely help to establish optimal conditions for STEM-EELS MDS studies, both theoretical and experimental.

IV. CONCLUSIONS

We have presented a study of simulated magnon diffuse scattering (MDS) in bcc Fe samples, of different thicknesses and temperatures, to explore the possibility of temperature-aided MDS detection in scanning transmission electron microscopy (STEM). An annular dark-field (ADF) detector that collects the relevant MDS signal surrounding the central Bragg disk [illustrated by the green dashed lines in Fig. 2(a)] has been employed.

It was found that when the effects of the atomic vibrations are neglected, the MDS signal I_{MDS} grows approximately linearly up to the Curie temperature (T_{C}) of Fe, presenting a much less-varying behavior for higher temperatures. Also, instead of increasing monotonically as a function of thickness, the MDS signal displayed an alternating behavior due to dynamical diffraction.

When the Debye-Waller factor (DWF) is considered, the linear growth of I_{MDS} gives place to an oscillatory behavior, which presents a predominant peak for each thickness. This peak increases and shifts to higher temperatures as the thickness increases.

In contrast, the thermal diffuse scattering (TDS), due to the atomic vibrations (phonons), presented a signal (I_{TDS}) that grows more linearly than I_{MDS} (with DWF), but still displayed appreciable dynamical diffraction effects. Moreover, it was found that I_{TDS} was five orders of magnitude greater than the corresponding I_{MDS}. Nevertheless, an analysis of the signal-to-noise ratio (SNR) showed that under realistic measurement conditions, the I_{MDS} signal can become a statistically significant contribution to the total scattering intensity. In particular, we found that SNR ≥ 3 can be achieved with existing STEM machines in less than 30 min. of data acquisition for a bcc Fe sample of 16.072 nm thickness at 500 K.

ACKNOWLEDGMENTS

We acknowledge the support of the Swedish Research Council, Olle Engkvist's foundation, Carl Trygger's Foundation, Knut and Alice Wallenberg Foundation, and eSSENCE for financial support. Simulations were enabled by resources provided by the Swedish National Infrastructure for Computing (SNIC) at NSC Centre partially funded by the Swedish Research Council through Grant Agreement No. 2018-05973. SuperSTEM is the National Research Facility for Advanced Electron Microscopy funded by the Engineering and Physical Sciences Research Council (EPSRC). We acknowledge financial support from the Engineering and Physical Sciences Research Council (EPSRC) via Grant No. EP/V048767/1 and Royal Society Grant No. IES/R1/211016. J.C.I. acknowledges the support of the Center for Nanophase Materials Sciences, which is a DOE Office of Science User Facility.

Appendix A: Convergence in terms of the averaging of snapshots

The accuracy of the inelastic signals $I_{\mathrm{ine}}(T)$ computed with Eq. (1) depends, in particular, on the number of snapshots N_s considered for the averaging process. A higher N_s produces a more converged value of $I_{\mathrm{ine}}(T)$.

Given a fixed N_s, it is relevant to estimate the degree of accuracy of the computed signals. A rough estimation can be achieved by exploiting the fact that the elastic signal $I_{\mathrm{ela}}(T)$ should consist of only Bragg disks.

Take for example Fig. 7, showing signals for bcc Fe of 20.09 nm thickness at 1700 K—including the Debye-Waller factor (DWF) and using the cutoff distance $r_{\mathrm{cut}} = 1$ nm (for information about the DWF and r_{cut}, please refer to the last two paragraphs of Section II). Specifically, in Fig. 7 we show I_{ela}/I_0 and I_{MDS}/I_0 (where I_0 denotes the intensity of the incident electron beam integrated over the whole diffraction plane) along a vertical profile through the center of the diffraction plane, i.e., as a function of the scattering angle θ_y, with $\theta_x = 0$. We have included vertical gray bars indicating the position and width of the Bragg disks.

It can be appreciated in Fig. 7 that there is a non-zero elastic signal between the Bragg disks. This signal, called hereafter $I_{\mathrm{error}}^{N_s}$, goes to zero as N_s increases. Hence, from Eq. (1), computing I_{MDS} with a given N_s gives an error on the order of $I_{\mathrm{error}}^{N_s}$ in the resulting MDS signal (outside the Bragg disks). In this work, in which $N_s = 101$, and in particular in Fig. 7, $I_{\mathrm{error}}^{N_s=101}$ is about two orders of magnitude smaller than the corresponding I_{MDS}. We include $I_{\mathrm{MDS}}/(100 I_0)$ in Fig. 7 (red curve) to help illustrate this result.

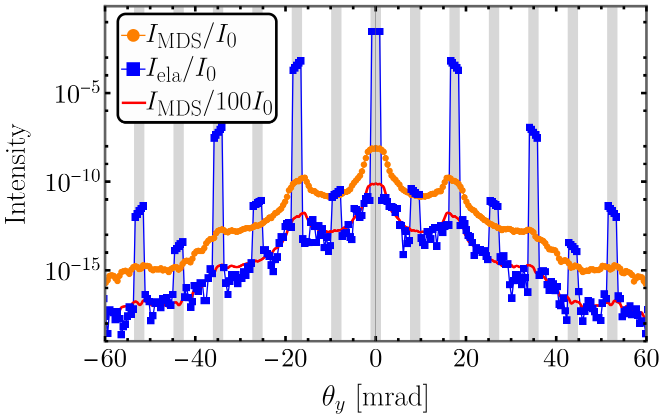

FIG. 7. Elastic and magnon diffuse scattering signals—$I_{\rm ela}$ and $I_{\rm MDS}$ (divided by the total intensity I_0 of the incident beam integrated over the whole diffraction plane), respectively [see Eq. (1)]—for bcc Fe of 20.09 nm thickness at 1700 K, including the Debye-Waller factor (DWF) and using the cutoff distance $r_{\rm cut} = 1$ nm. A curve of $I_{\rm MDS}/I_0$ divided by 100 is included for comparison with $I_{\rm ela}$. The position and width of the Bragg disks are indicated by the vertical gray bars.

Appendix B: Mean square displacements

The mean-squared displacement (MSD) used for the implementation of Debye-Waller factors [11] at temperature T are given in Table I, along with the lattice parameter of bcc Fe, as obtained by molecular dynamics calculations.

TABLE I. Mean-squared displacement (MSD)—used for the implementation of Debye-Waller factors—and bcc Fe lattice parameter a, at temperature T, used for TDS calculations.

T [K]	a [Å]	MSD [Å^2]	T [K]	a [Å]	MSD [Å^2]
100	2.855389	0.004693	1000	2.881882	0.061313
200	2.856854	0.009678	1100	2.886190	0.069974
300	2.858989	0.014849	1200	2.890794	0.079865
400	2.861494	0.020589	1300	2.895650	0.090492
500	2.864269	0.026535	1400	2.900800	0.102204
600	2.867294	0.032765	1500	2.906238	0.115404
700	2.870572	0.038693	1600	2.912003	0.130029
800	2.874080	0.045774	1700	2.918126	0.148881
900	2.877857	0.053119			

Appendix C: Convergence in terms of $r_{\rm cut}$

The microscopic electromagnetic fields $V(\mathbf{r})$, $\mathbf{B}(\mathbf{r})$, and $\mathbf{A}(\mathbf{r})$ of an atom vanish as the distance from the atom increases. Therefore, it is customary to define a cutoff distance $r_{\rm cut}$ above which these fields are set to zero to economize computational resources in crystals simulations. This establishes a compromise between the precision of a calculation and its computational resources demand.

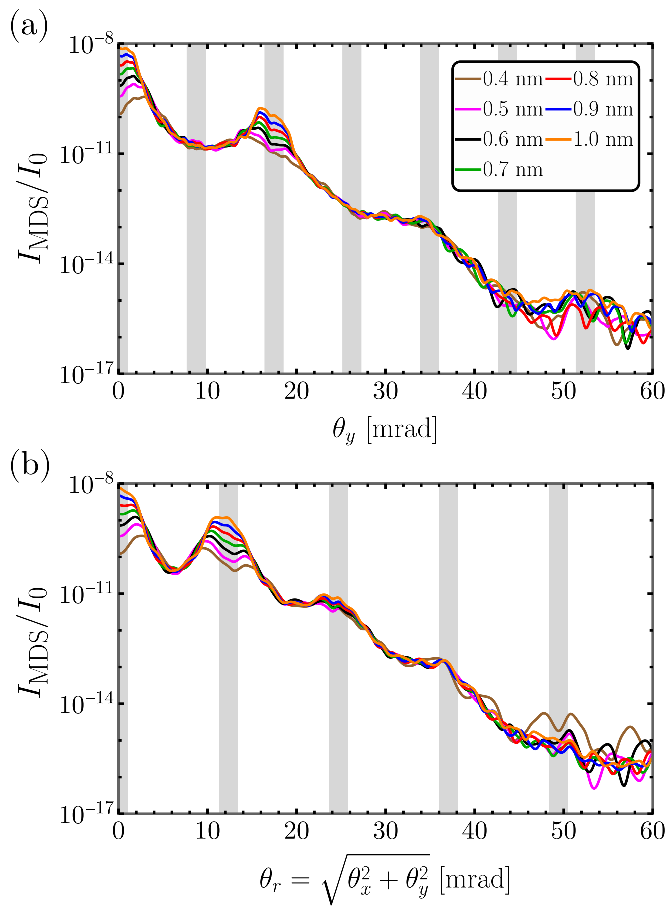

FIG. 8. Convergence of the magnon diffuse scattering signal $I_{\rm MDS}$ (divided by the intensity I_0 of the incident beam) for different cutoff distances $r_{\rm cut}$—indicated in the inset of the top plot [Fig. 8(a)]—for bcc Fe of 20.09 nm thickness at 1700 K, including the Debye-Waller factor (DWF). (a) Vertical [i.e., as a function of the scattering angle θ_y for fixed $\theta_x = 0$] and (b) diagonal [i.e., as a function of $\theta_r = \sqrt{\theta_x^2+\theta_y^2}$, with $\theta_x = \theta_y$] profiles through the origin of the diffraction plane. The gray bars indicate the position and width of the Bragg disks.

To show the convergence level of our calculations, in Fig. 8 we show MDS profiles (in logarithmic scale) for different values of $r_{\rm cut}$, as a function of the scattering angle θ_r, for bcc Fe of 20.09 nm thickness, at 1700 K, including the DWF. Specifically, in Fig. 8(a) we show the vertical profile of $I_{\rm MDS}/I_0$ (I_0 denotes the intensity of the incident electron beam) through the origin of the diffraction plane—that is, as a function of θ_y for fixed $\theta_x = 0$. Meanwhile, Fig. 8(b) shows a diagonal profile of $I_{\rm MDS}/I_0$ through the origin of the diffraction plane—i.e., as a function of $\theta_r = \sqrt{\theta_x^2+\theta_y^2}$ with $\theta_x = \theta_y$. We have included vertical gray bars indicating the position and width of the Bragg disks in both Figs. 8(a) and 8(b).

It can be observed in these figures that the MDS signal decreases as the scattering angle increases, presenting maxima near the position of the high-intensity Bragg disks (in agreement with Figs. 2(a), 2(b), and 7). Moreover, the highest MDS signal is located around the central Bragg spot (at zero scattering angle), in conformity with Ref. [9]. Therefore, in our study, we considered an annular dark-field (ADF) detector [17] of outer collection semiangle 7 mrad and inner collection semiangle 2 mrad [represented by the green dashed lines in Fig. 2(a)] to avoid all Bragg disks.

In particular, well converged MDS signals within the considered ADF detector can be obtained with $r_{\mathrm{cut}} = 0.4$ nm, as shown Figs. 8(a) and 8(b). However, to better resolve the MDS near and within the Bragg disks, a higher r_{cut} is necessary.

[1] C. B. Carter and D. B. Williams, *Transmission Electron Microscopy: A Textbook for Materials Science* (Springer, 2009).
[2] O. L. Krivanek, T. C. Lovejoy, N. Dellby, T. Aoki, R. Carpenter, P. Rez, E. Soignard, J. Zhu, P. E. Batson, M. J. Lagos, R. F. Egerton, and P. A. Crozier, Nature **514**, 209 (2014).
[3] O. Krivanek, N. Dellby, J. Hachtel, J.-C. Idrobo, M. Hotz, B. Plotkin-Swing, N. Bacon, A. Bleloch, G. Corbin, M. Hoffman, C. Meyer, and T. Lovejoy, Ultramicroscopy **203**, 60 (2019).
[4] N. Dellby, T. Lovejoy, G. Corbin, N. Johnson, R. Hayner, M. Hoffman, P. Hrncrik, B. Plotkin-Swing, D. Taylor, and O. Krivanek, Microscopy and Microanalysis **26**, 1804 (2020).
[5] N. Dellby, O. Krivanek, N. Bacon, G. Corbin, N. Johnson, R. Hayner, P. Hrncrik, B. Plotkin-Swing, D. Taylor, Z. Szilaygi, and T. Lovejoy, Microscopy and Microanalysis **28**, 2640 (2022).
[6] M. J. Lagos, I. C. Bicket, S. S. Mousavi M., and G. A. Botton, Microscopy **71**, i174 (2022).
[7] K. Lyon, A. Bergman, P. Zeiger, D. Kepaptsoglou, Q. M. Ramasse, J. C. Idrobo, and J. Rusz, Phys. Rev. B **104**, 214418 (2021).
[8] B. Mendis, Ultramicroscopy **230**, 113390 (2021).
[9] B. Mendis, Ultramicroscopy **239**, 113548 (2022).
[10] O. Eriksson, A. Bergman, L. Bergqvist, and J. Hellsvik, *Atomistic Spin Dynamics: Foundations and Applications* (Oxford University Press, 2017).
[11] C. Kittel and P. McEuen, *Introduction to Solid State Physics* (John Wiley & Sons, 2018).
[12] P. Mohn, *Magnetism in the Solid State* (Springer Science & Business Media, 2006).
[13] I. Žutić, J. Fabian, and S. Das Sarma, Rev. Mod. Phys. **76**, 323 (2004).
[14] F. Pulizzi, Nature materials **11**, 367 (2012).
[15] A. Barman, G. Gubbiotti, S. Ladak, A. O. Adeyeye, M. Krawczyk, J. Gräfe, C. Adelmann, S. Cotofana, A. Naeemi, V. I. Vasyuchka, B. Hillebrands, S. A. Nikitov, H. Yu, D. Grundler, A. V. Sadovnikov, A. A. Grachev, S. E. Sheshukova, J.-Y. Duquesne, M. Marangolo, G. Csaba, W. Porod, V. E. Demidov, S. Urazhdin, S. O. Demokritov, E. Albisetti, D. Petti, R. Bertacco, H. Schultheiss, V. V. Kruglyak, V. D. Poimanov, S. Sahoo, J. Sinha, H. Yang, M. Münzenberg, T. Moriyama, S. Mizukami, P. Landeros, R. A. Gallardo, G. Carlotti, J.-V. Kim, R. L. Stamps, R. E. Camley, B. Rana, Y. Otani, W. Yu, T. Yu, G. E. W. Bauer, C. Back, G. S. Uhrig, O. V. Dobrovolskiy, B. Budinska, H. Qin, S. van Dijken, A. V. Chumak, A. Khitun, D. E. Nikonov, I. A. Young, B. W. Zingsem, and M. Winklhofer, Journal of Physics: Condensed Matter **33**, 413001 (2021).
[16] R. F. Loane, P. Xu, and J. Silcox, Acta Crystallographica Section A **47**, 267 (1991).
[17] E. J. Kirkland, *Advanced Computing in Electron Microscopy* (Springer, 2010).
[18] A. Edström, A. Lubk, and J. Rusz, Phys. Rev. B **94**, 174414 (2016).
[19] A. Edström, A. Lubk, and J. Rusz, Phys. Rev. Lett. **116**, 127203 (2016).
[20] P. M. Zeiger and J. Rusz, Phys. Rev. Lett. **124**, 025501 (2020).
[21] D. Van Dyck, Ultramicroscopy **109**, 677 (2009).
[22] B. D. Forbes, A. V. Martin, S. D. Findlay, A. J. D'Alfonso, and L. J. Allen, Phys. Rev. B **82**, 104103 (2010).
[23] K. Zakeri, Y. Zhang, and J. Kirschner, Journal of Electron Spectroscopy and Related Phenomena **189**, 157 (2013).
[24] The Uppsala atomistic spin dynamics code, `UppASD`, `https://github.com/UppASD/UppASD` (2023), last accessed 2023-01-30.
[25] H. Ebert, D. Ködderitzsch, and J. Minár, Reports on Progress in Physics **74**, 096501 (2011).
[26] The Large-scale Atomic/Molecular Massively Parallel Simulator (LAMMPS), `https://www.lammps.org`, last accessed 2023-01-30.
[27] A. P. Thompson, H. M. Aktulga, R. Berger, D. S. Bolintineanu, W. M. Brown, P. S. Crozier, P. J. in 't Veld, A. Kohlmeyer, S. G. Moore, T. D. Nguyen, R. Shan, M. J. Stevens, J. Tranchida, C. Trott, and S. J. Plimpton, Comp. Phys. Comm. **271**, 108171 (2022).
[28] We have used `LAMMPS` version 23 Jun 2022 – Update 1.
[29] M. I. Mendelev, S. Han, D. J. Srolovitz, G. J. Ackland, D. Y. Sun, and M. Asta, Philosophical Magazine **83**, 3977 (2003).
[30] K. Lyon and J. Rusz, Acta Crystallographica Section A **77**, 509 (2021).
[31] L.-M. Peng, G. Ren, S. L. Dudarev, and M. J. Whelan, Acta Crystallographica Section A **52**, 257 (1996).
[32] J. Snarski-Adamski, A. Edström, P. Zeiger, J. Ángel Castellanos-Reyes, K. Lyon, M. Werwiński, and J. Rusz, Ultramicroscopy **247**, 113698 (2023).
[33] C. B. Carter and D. B. Williams, *Transmission Electron Microscopy: Diffraction, Imaging, and Spectrometry* (Springer, 2016).
[34] A. Rose, *Vision: Human and Electronic* (Springer, 1973).
[35] F. Houdellier, L. de Knoop, C. Gatel, A. Masseboeuf, S. Mamishin, Y. Taniguchi, M. Delmas, M. Monthioux, M. Hÿtch, and E. Snoeck, Ultramicroscopy **151**, 107 (2015), special Issue: 80th Birthday of Harald Rose; PICO 2015 – Third Conference on Frontiers of Aberration Corrected Electron Microscopy.

[36] X. Shao, A. Srinivasan, W. K. Ang, and A. Khursheed, Nature communications **9**, 1288 (2018).

[37] S. Konings and M. Bischoff, Microscopy and Microanalysis **26**, 566–567 (2020).